European Biophysics Journal
https://doi.org/10.1007/s00249-020-01473-6

ORIGINAL ARTICLE

Following the footprints of variability during filopodial growth

Daniela Senra[1] · Alejandra Páez[2,3,4] · Geraldine Gueron[2,3] · Luciana Bruno[5] · Nara Guisoni[1]

Received: 3 August 2020 / Revised: 6 October 2020 / Accepted: 19 October 2020

Abstract
Filopodia are actin-built finger-like dynamic structures that protrude from the cell cortex. These structures can sense the environment and play key roles in migration and cell–cell interactions. The growth-retraction cycle of filopodia is a complex process exquisitely regulated by intra- and extra-cellular cues, whose nature remains elusive. Filopodia present wide variation in length, lifetime and growth rate. Here, we investigate the features of filopodia patterns in fixed prostate tumor cells by confocal microscopy. Analysis of almost a thousand filopodia suggests the presence of two different populations: one characterized by a narrow distribution of lengths and the other with a much more variable pattern with very long filopodia. We explore a stochastic model of filopodial growth which takes into account diffusion and reactions involving actin and the regulatory proteins formin and capping, and retrograde flow. Interestingly, we found an inverse dependence between the filopodial length and the retrograde velocity. This result led us to propose that variations in the retrograde velocity could explain the experimental lengths observed for these tumor cells. In this sense, one population involves a wider range of retrograde velocities than the other population, and also includes low values of this velocity. It has been hypothesized that cells would be able to regulate retrograde flow as a mechanism to control filopodial length. Thus, we propound that the experimental filopodia pattern is the result of differential retrograde velocities originated from heterogeneous signaling due to cell–substrate interactions or prior cell–cell contacts.

Keywords Filopodial growth · Stochastic model · Actin · Regulatory proteins · Fluorescence microscopy · Prostate tumor cells

Introduction

Filopodia are filamentous cell projections that protrude from the plasma membrane by the polymerization of actin filaments. Filopodia are well-conserved structures, present in diverse cell systems and known to play a key role in cell migration, sensing and cell–cell communication (Mattila and Lappalainen 2008; Cohen et al. 2010). Typically, a filopodium contains a bundle of around 10–30 actin filaments (Bornschlögl 2013) and grows at a speed of 0.01–0.2 μm/s (Steffen et al. 2006), reaching lengths of a few micrometers (Jontes et al. 2000; Husainy et al. 2010; Marchenko et al. 2017). As a consequence of the complex processes involved in filopodia dynamics there are wide variations in filopodial

We acknowledge support from the Agencia Nacional de Promoción Científica y Tecnológica (PICT 2015-0370 and PICT-RAICES-2018-02639), Argentina.

✉ Nara Guisoni
naraguisoni@conicet.gov.ar

Luciana Bruno
lbruno@df.uba.ar

[1] Instituto de Investigaciones Fisicoquímicas Teóricas y Aplicadas, Universidad Nacional de La Plata, CONICET, La Plata, Argentina

[2] Laboratorio de Inflamación y Cáncer, Departamento de Química Biológica, Facultad de Ciencias Exactas y Naturales, Universidad de Buenos Aires, C1428EGA Buenos Aires, Argentina

[3] CONICET, Universidad de Buenos Aires, Instituto de Química Biológica de la Facultad de Ciencias Exactas y Naturales (IQUIBICEN), C1428EGA Buenos Aires, Argentina

[4] Unidad de Transferencia Genética, Instituto de Oncología "Ángel H. Roffo", Universidad de Buenos Aires, Buenos Aires, Argentina

[5] Instituto de Cálculo, Facultad de Ciencias Exactas y Naturales, Universidad de Buenos Aires, CONICET, Pabellón 2, Ciudad Universitaria (1428), Buenos Aires, Argentina

Published online: 03 November 2020

lifetimes, ranging from a few seconds to several minutes (Heckman and Plummer 2013).

The mechanisms of filopodia initiation are still not clear. It has been proposed that filopodia would emerge as a consequence of the reorganization of the lamellipodial actin network upon the convergent elongation of privileged filaments, which would bind a complex of molecules to their barbed ends allowing them to continue elongating together (Svitkina et al. 2003). On the contrary, other authors (Steffen et al. 2006; Paul et al. 2015) found that filopodia are able to form in the absence of lamellipodia suggesting different functionality between both actin structures.

Once initiated, the bundle of actin filaments elongates by the polymerization of actin monomers at the filaments barbed ends and retracts as a consequence of both, depolymerization and retrograde flow. Filopodia extension and retraction is a dynamic process controlled by different proteins, including capping protein and formin (Shekhar et al. 2015). These regulators have opposite effects on the filopodial length: while formin accelerates actin assembly, capping protein prevents its polymerization (Goode and Eck 2007; Sinnar et al. 2014). Both proteins bind actin barbed ends with high affinity and slow dissociation, which initially led to the conclusion that they were mutually exclusive (Shekhar et al. 2015; Kovar et al. 2005). However, it has been recently shown that formin and capping proteins are able to simultaneously bind barbed ends and coregulate filament assembly (Shekhar et al. 2015).

It has been suggested that retrograde flow in the cell cortex at the base of the filopodium is the main retraction mechanism, which also generates retrograde forces on the substrate (Bornschlögl et al. 2013). Retrograde flow originates from the combination of two processes: the actin treadmilling due to the depolymerization at the rear part of the filopodium and the action of myosin motors (Lin et al. 1996; Anderson et al. 2008). For example, it has been found that filopodium elongated more that 80% after inhibition of myosin II in neuronal growth cones (Medeiros et al. 2006). Depolymerization of actin at the tip can also contribute to the retrograde flow in melanoma cells and fibroblasts in a process regulated by cofilin and fascin (Breitsprecher et al. 2011).

The magnitude of the retrograde flow depends on the cell type and species; values in the range 5–260 nm/s have been reported (see references in Table 1 in Bornschlögl (2013)). Furthermore, its value might also depend on the state of development of the filopodia (Tatavarty et al. 2012), on probes acting as guidance cues to their growth stabilizing or destabilizing filopodia (Gallo and Letourneau 2004; Saha et al. 2016; Jacquemet et al. 2016, 2019) and/or on the substrate stiffness (Liou et al. 2014).

The complexity of the mechanisms underlying the initiation, maintenance, and retraction of filopodia has inspired theoretical and computational approaches for a better understanding of the biological system. Regarding filopodial growth, several authors have addressed this issue, using deterministic analytical models (Marchenko et al. 2017; Mogilner and Rubinstein 2005; Daniels 2010; Wolff et al. 2014) and stochastic simulations (Lan and Papoian 2008; Zhuravlev and Papoian 2009; Erban et al. 2014; Atilgan et al. 2006). In a groundbreaking publication, Mogilner and Rubinstein (2005) propose a deterministic one-dimensional reaction-diffusion model for G-actin dynamics within filopodia. Some characteristic scales of filopodia emerge from the model, such as the typical filopodial length (of the order of few microns) and that more than 10 bundled filaments are required to avoid buckling. Other authors propose mean-field models that also account for the effect of myosin motors (Marchenko et al. 2017; Wolff et al. 2014) and capping proteins (Daniels 2010). On the other hand, Papoian's group has made a significant contribution to the stochastic modeling of filopodial growth (Lan and Papoian 2008; Zhuravlev and Papoian 2009; Erban et al. 2014; Zhuravlev and Papoian 2011). In this way, Lan and Papoian (2008) developed a one-dimensional model for a bundle of filaments within a filopodium. They consider the polymerization and depolymerization of actin at the barbed end, as well as an effective retrograde velocity for each filament individually. The model allows to observe an equilibrium state with fluctuations around the stationary length. Zhuravlev and Papoian (2009) brings complexity to this model, by adding the regulatory effect of capping proteins and formins. Interestingly, considering actin-binding proteins amplifies molecular noise and eventually leads to large growth-retraction oscillations in the filopodial lengths.

In this paper, we study the pattern distribution of filopodial lengths by means of a stochastic model based in the work of Zhuravlev and Papoian (2009), though considering recent results showing that formin and capping proteins coregulate the actin assembly (Shekhar et al. 2015). It has been hypothesized that cells can control different processes such as migration or the establishment of cell–cell contacts by regulating the retrograde flow and, as a consequence, the length and stability of filopodia (Gallo and Letourneau 2004; Jacquemet et al. 2016; Liou et al. 2014). Thus, we explore in silico the effect of varying the magnitude of the retrograde flow on the mean filopodial length and, more importantly, on its dispersion. We compare the results of the numerical simulations with the filopodial lengths obtained from the inspection of filopodia in fixed cultured prostate tumor cells. Our results suggest that the experimental data would consist of at least two populations of filopodia characterized by different retrograde velocities. The biological significance of our results is also discussed.

Results

Stochastic model of filopodial growth

We study filopodial growth dynamics by considering a stochastic reaction–diffusion model. The model used here is similar to that proposed by Zhuravlev and Papoian (2009). A growing filopodium generates a region that is an extension of the cytoplasm where actin, formin and capping molecules can react and diffuse (see Fig. 1a). Using a molecular approach (Erban et al. 2014), the chemical reactions at the filament barbed end are explicitly considered. The depolymerization at the filament pointed end as well as the action of the myosin motors are considered as an effective process that regulates filopodial retraction. The diffusion of the distinct molecules into the cytoplasmic extension is taken into account explicitly.

Following the model proposed by Zhuravlev and Papoian (2009), the filopodial structure is built with actin molecules as building blocks: G-actin polymerizes into F-actin at the filament barbed end. Actin depolymerization of the filament barbed end is also possible. These processes occur with rates $k_{\text{on}}^{\text{act}}$ and $k_{\text{off}}^{\text{act}}$, respectively. Formin and capping proteins can also bind at the filament barbed end, noticeably affecting G-actin polymerization. In this way, while capping of the filaments blocks actin polymerization, formin enhances substantially filament assembly (Goode and Eck 2007; Sinnar et al. 2014). Therefore, if $k_{\text{on}}^{\text{act-form}}$ is the actin polymerization rate when a formin molecule is already bound to the filament, we consider that $k_{\text{on}}^{\text{act-form}} \sim 5k_{\text{on}}^{\text{act}}$ (Kovar et al. 2006). In our model, we also considered recent results showing that formin and capping proteins can coregulate filament assembly by simultaneous binding to the barbed end (Shekhar et al. 2015). This aspect was not taken into account by Zhuravlev and Papoian (2009), who assumed that formin and capping were mutually exclusive. However, Shekhar et al. (2015) found that the on- and off-rates of formin (capping) are affected by the presence of the capping (formin) protein (Shekhar et al. 2015). We allow for these results by defining new values for the binding and unbinding rates $k_{\text{on}}^{\text{form-cap}}$ and $k_{\text{off}}^{\text{form-cap}}$ for the binding of formin when a capping molecule is already bound to the filament, and $k_{\text{on}}^{\text{cap-form}}$ and $k_{\text{off}}^{\text{cap-form}}$ for the corresponding capping case. The high affinity and slow

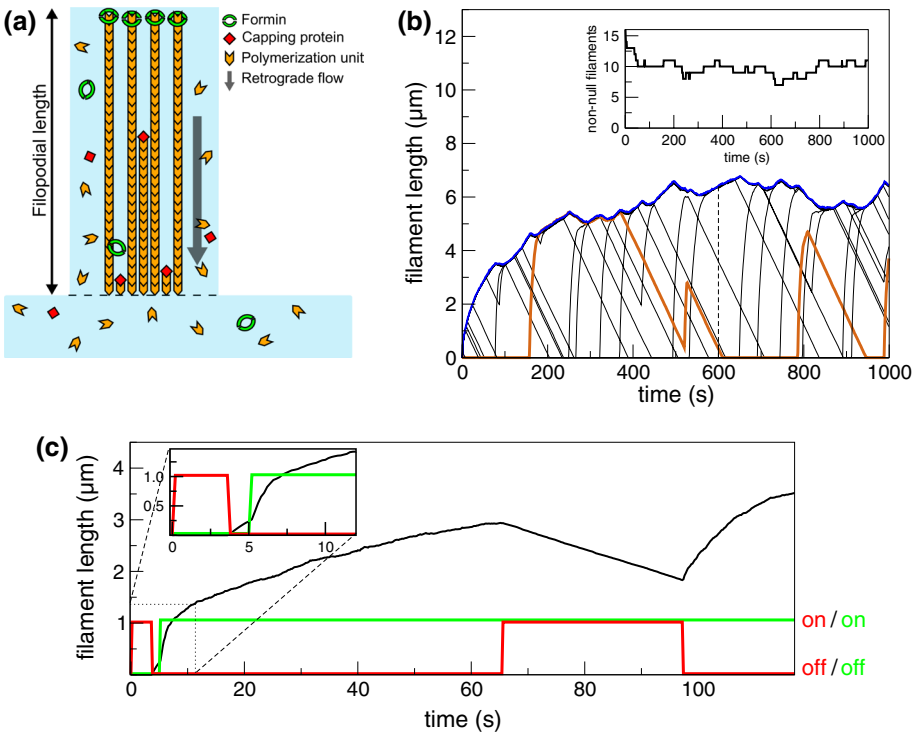

Fig. 1 **a** Schematic representation of the model for filopodial growth. **b** Filaments within a filopodium length and filaments with non-null length (inset) as a function of time for $v_r = 30$ nm/s. The filopodium length corresponds to the largest filament (blue line). As an example, for 600 s (dashed line) there are two short filaments, one with intermediate length, and several ones with maximum length [schematically illustrated in (**a**)]. The orange line highlights the dynamics of a single filament, showing that it can disappear and grow again from the cytoplasm. **c** Filament length and binding/unbinding of formin and capping molecules (black, green and red, respectively), as a function of time for $v_r = 10$ nm/s. Formin increases the growing filament velocity (~5 s), whereas capping blocks filament polymerization, and the length decreases due to the retrograde flow. In the time interval between 65 and 97 s both formin and capping are bound. Inset: enlargement of short time region

dissociation of formins and capping proteins to the barbed end are reflected in the values of the on- and off-rates of these molecules, as can be seen in Table 1.

G-actin, formin and capping molecules cytosolic concentrations are considered to be constant, with bulk values $[A]_{cyt}$, $[F]_{cyt}$ and $[C]_{cyt}$, respectively (Zhuravlev and Papoian 2009; Mogilner and Rubinstein 2005). These molecules are able to diffuse into the cytoplasmic extension with effective diffusion coefficients D_{act}, D_{form} and D_{cap} (Mogilner and Rubinstein 2005; McGrath et al. 1998; Vitriol et al. 2015; McMillen and Vavylonis 2016; Kapustina et al. 2010). This is another difference in relation to the work of Zhuravlev and Papoian (2009), which does not take into account the diffusion of formin and capping molecules. Formin diffusion rate was considered with the same value as actin since both have similar molecular weight. Finally, the depolymerization of actin at the pointed end coupled with the action of myosins are taken into account as an effective process that regulates filopodial retraction. In this way, we assume a constant retrograde velocity whose action is to continually shorten the filaments, as made previously (Lan and Papoian 2008; Zhuravlev and Papoian 2009; Erban et al. 2014).

Despite that an actin filament is composed of two protofilaments (Dominguez and Holmes 2011), we model each filament as a rodlike structure without contemplating its internal double stranded helical organization, as it was also considered in previous works (Mogilner and Rubinstein 2005; Lan and Papoian 2008; Zhuravlev and Papoian 2009; Erban et al. 2014; Zhuravlev and Papoian 2011; Peskin et al. 1993). The successive binding of actin molecules makes the filament length increase by a polymerization unit, as schematically shown in Fig. 1a. Also, we consider that a bundle of filaments constitutes a filopodia, with a maximum number of 16. The filopodial length is equal to the largest filament length (Fig. 1a, b). We use a stochastic molecular approach to simulate reactions and diffusion in our model (Erban et al.

Table 1 Parameters used in the model simulations

	Values	References
Diffusion rates		
Actin	$D_{act} = 5\mu m^2 s^{-1}$	Mogilner and Rubinstein (2005), McGrath et al. (1998), Vitriol et al. (2015)
Formin	$D_{form} = 5\mu m^2 s^{-1}$	–
Capping	$D_{cap} = 5\mu m^2 s^{-1}$	McMillen and Vavylonis (2016), Kapustina et al. (2010)
Actin		
Polymerization free barbed end	$k_{on}^{act} = 11.6\mu M^{-1}s^{-1}(21.9s^{-1})^*$	Zhuravlev and Papoian (2009), Pollard et al. (2000)
Polymerization formin-anti-capped barbed end	$k_{on}^{act\text{-}form} = 53\mu M^{-1}s^{-1}(100s^{-1})^*$	Zhuravlev and Papoian (2009), Kovar et al. (2006)
Depolymerization	$k_{off}^{act} = 1.4s^{-1}$	Zhuravlev and Papoian (2009), Pollard et al. (2000)
Formin		
On-rate free barbed end	$k_{on}^{form} = 29.1\mu M^{-1}s^{-1}(54.9s^{-1})^*$	Shekhar et al. (2015)
On-rate capping barbed end	$k_{on}^{form\text{-}cap} = 1.6\mu M^{-1}s^{-1}(3.02s^{-1})^*$	Shekhar et al. (2015)
Off-rate free barbed end	$k_{off}^{form} = 8.1 \times 10^{-5}s^{-1}$	Shekhar et al. (2015)
Off-rate capping barbed end	$k_{off}^{form\text{-}cap} = 5.6 \times 10^{-3}s^{-1}$	Shekhar et al. (2015)
Capping molecule		
On-rate free barbed end	$k_{on}^{cap} = 12.8\mu M^{-1}s^{-1}(24.2s^{-1})^*$	Shekhar et al. (2015)
On-rate formin barbed end	$k_{on}^{cap\text{-}form} = 0.145\mu M^{-1}s^{-1}(0.27s^{-1})^*$	Shekhar et al. (2015)
Off-rate free barbed end	$k_{off}^{cap} = 2.0 \times 10^{-4}s^{-1}$	Shekhar et al. (2015)
Off-rate formin barbed end	$k_{off}^{cap\text{-}form} = 3.3 \times 10^{-3}s^{-1}$	Shekhar et al. (2015)
Cytosolic concentrations		
Actin	$[A]_{cyt} = 10\mu M$	Zhuravlev and Papoian (2009), Mogilner and Rubinstein (2005)
Capping protein	$[C]_{cyt} = 50$ nM	(Zhuravlev and Papoian 2009)
Formin	$[F]_{cyt} = 80$ nM	Zhuravlev and Papoian (2009)
Retrograde flow speed	$v_r \in [5, 100]$ nm/s	Bornschlögl (2013)
Polymerization unit	$\delta = 2.7$ nm	Mogilner and Rubinstein (2005), Zhuravlev and Papoian (2009), Peskin et al. (1993)
Maximum number of filaments	$N_{max} = 16$	Zhuravlev and Papoian (2009)

*Reaction rates per molecule are presented in parentheses in units of s^{-1} (needed for the stochastic molecular simulations performed). For details, see Sect. 4.1

2014), as discussed in Section "Numerical simulations". The parameters used in the model are given in Table 1. It should be noted that all the on- and off-rates, the actin cytosolic concentration, the actin and capping protein diffusion rates, the actin monomer size, the range of retrograde velocity and the maximum number of filaments in a filopodium were determined experimentally.

To give some insight into how the model works, a representative filament temporal evolution is shown in Fig. 1c. As expected, the growth velocity of the filament is notably increased by the binding of a formin, as can be seen in the inset of Fig. 1c. On the other hand, when a capping molecule binds to the filament, polymerization stops and the filament retracts linearly as a consequence of the retrograde velocity.

Figure 1b shows an example of the dynamic of the filaments within a filopodium. The number of filaments with non-null length is shown in the inset. According to the model, the filopodial growth rate is high for short times, but as time goes on, the velocity decreases exponentially. This result is in agreement with the deterministic model proposed by Mogilner and Rubinstein (2005). In fact, for longer times, a balance between the actin polymerization and the retrograde velocity leads to a stationary length. This result is in accordance with the fact that the number of non-null filaments tends to an average value (inset of Fig. 1b). As can be seen in Fig. 1b, if one filament disappears by the continuous binding of a capping molecule, it is able to grow again from the cytoplasm. Notably, the stochastic binding/unbinding of formin and capping molecules results in high variability in filopodial length (also observed in Zhuravlev and Papoian 2009), as compared to models where only actin polymerization/depolymerization is taken into account (Lan and Papoian 2008; Erban et al. 2014).

The filopodial length is obviously affected by the model parameters. An elegant mean field expression for the steady-state filopodium length was obtained for models where only actin polymerization/depolymerization is considered (Lan and Papoian 2008; Zhuravlev and Papoian 2011). These authors found that the stationary length increases linearly with both the actin diffusion coefficient and the actin cytosolic concentration. Their results also showed that the steady-state filopodium length presents a nonlinear increase with the binding rate of actin and a nonlinear decrease with both the retrograde velocity and the number of filaments. Finally, the stationary filopodium length is not significantly influenced by actin depolymerization. We expect that these results would be qualitatively valid for our model.

Here we are interested in studying the effect of varying the model parameters that may be involved in the regulation of filopodia growth. We assume that biochemical processes intrinsic to the cell, such as polymerization/depolymerization rates, diffusion coefficients, cytosolic concentrations, and the number of filaments in a filopodium, will not be highly variable among cells with a common identity. On the other hand, it has been shown that heterogeneous signaling induced variability in the retrograde velocity (Gallo and Letourneau 2004; Jacquemet et al. 2016, 2019; Liou et al. 2014). These experimental results indicate that the retrograde flow can work as a control mechanism of filopodial growth and retraction. The sensitive nonlinear behavior of the stationary filopodial length with the retrograde velocity observed for simpler models (Lan and Papoian 2008) reinforces this election. Therefore, we will explore the effect of varying the retrograde velocity throughout the simulations.

Influence of retrograde velocity in filopodial length

To explore the effect of the retrograde flow on the filopodial lengths, we run simulations varying the retrograde velocity (v_r) while keeping the rest of the parameter values unchanged (Table 1). Figure 2a displays the results for 3 different values of v_r in the range between 10 and 100 nm/s. For each value of v_r, Fig. 2a presents several individual simulations, as well as the filopodial length averaged over these curves (for a definition see Eq. 3 in Section "Statistical analysis"). Our simulations go up to $t = 1000$ s, since the average filopodia lifetime is reported to be in the order of a few minutes (Jontes et al. 2000; Miller et al. 1995; Jacquemet

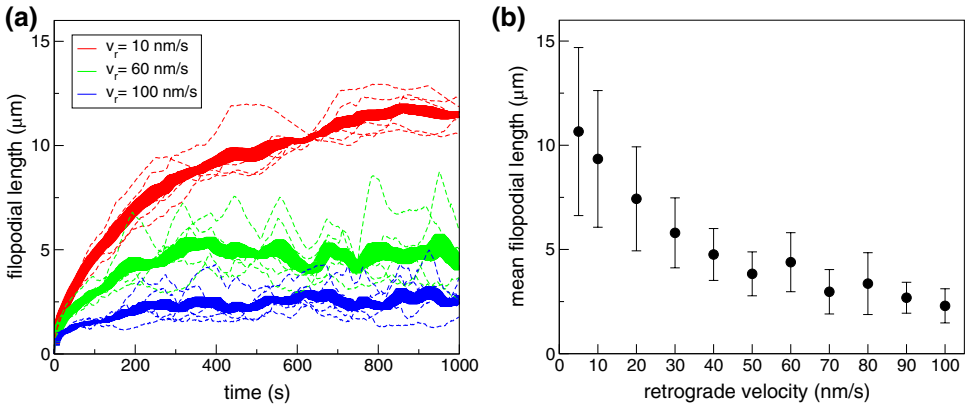

Fig. 2 **a** Filopodial length (dashed lines) for different retrograde velocities v_r, as indicated. For each value of v_r the solid line represents the filopodial length averaged over the 5 runs, $\langle L(t) \rangle$, and the thickness of the line depicts the standard error. **b** Mean filopodial length $\overline{L}$ as a function of v_r. The error bars represent the standard deviation. Further information about simulation data can be found in Section "Statistical analysis"

et al. 2017), even though some filopodia are longer lived (Miller et al. 1995; Jacquemet et al. 2017; McCroskery et al. 2006). Interestingly, the time course of individual filopodial lengths shows large fluctuations, and different simulations for the same parameter values are also very variable. The reason for such behaviour lies on the stochastic nature of the binding/unbinding of actin and regulatory proteins, taken into account by the model. We verified that larger values of v_r resulted in shorter lengths. It can also be observed that for low values of v_r, the filopodial length presents a larger transient towards the stationary length. Also, the filopodium growth rate (estimated from the average speed at each simulation time step in the short time region, see Fig. 2a) is of the order of 100 nm/s, comparable with the reported values (Steffen et al. 2006).

Many experiments deal with images of fixed cells (Jontes et al. 2000; Husainy et al. 2010; Paez et al. 2017; Oldenbourg et al. 2000), which display the distribution of filopodia at arbitrary moments in their lifetimes. To take this type of data into account, we will consider the full-time behaviour of filopodial length given by the model, instead of only the stationary value, as it was previously done in other theoretical works (Lan and Papoian 2008). Therefore, we compute the average of the filopodial lengths over both time and different realizations as an estimate of the mean filopodial length (Eq. 4 in Section "Statistical analysis"). Figure 2b shows that the mean filopodial length exhibits a nonlinear inverse dependence on the retrograde velocity. Then larger values of v_r result in shorter filopodia. Furthermore, it can be seen that the mean filopodial length is much more sensitive to variations of v_r for low values of retrograde velocity than for higher ones. The large dispersion in the mean filopodial length observed in Fig. 2b for low values of v_r is associated with the existence of a long transient to reach the equilibrium length (see Fig. 2a).

Filopodia in PC3 cells

To explore filopodia patterns, we studied cultured prostate tumor cells (PC3 cells) (Paez et al. 2017). The in vitro experiments were performed with cells growing on plastic culture wells previously coated with FNC coating mix (Athena Enzyme Systems). As described by the manufacturer, this formula resembles the extracellular matrix (ECM). After being fixated and stained for actin with rhodamine phalloidin, cells were imaged by confocal microscopy, as described in Section "Cell culture, sample preparation for imaging and confocal microscopy". While this condition has the advantage of allowing inspection of all the cells in the field with little noise, it has the drawback that the dynamical behavior of filopodia cannot be explored. However, these images are representative of the distribution of cells and filopodia in an arbitrary moment of their cycle. The images were analyzed with custom-made routines. A detailed description of the image analysis can be found in Section "Filopodia localization and tracking".

We show PC3 cultured cells imaged using phase contrast optics in Fig. 3a. The micrograph in Fig. 3b corresponds to the fluorescence channel and in Fig. 3c, we exhibit an overlay of both images. Since filopodia are easily distinguished in the fluorescence images, we found it more convenient to use these images for our analysis.

We focused on individual filopodia and not on filopodia located at cell–cell junctions or that form bridge-like structures, such as those described in Hoelzle and Svitkina (2012). Thus, we identified membrane regions where filopodia represented clearly delimited structures, while cell–cell protrusions and extremely dense regions were excluded for the analysis, similar to Jacquemet et al. (2017). Furthermore, filopodia with low signal to noise ratio (low intensity with respect to the background) and/or intermittent intensity levels that might correspond to protrusions that enter and go out the image plane were considered unfit to be measured. Figure 3d shows an example where the discarded areas were delimited by red rectangles and the trackable regions were circumscribed by green shapes.

We sampled filopodia from the trackable zones, generally one or two regions per cell were explored. We identified individual filopodia from the fluorescence images and manually delineated them (Fig. 3e) to acquire intensity profiles (Fig. 3f). We input the collected intensity profiles into a custom made program which determines the filopodial tip and base locations for each profile and computes the filopodial length by subtracking them. Thereby, we measured the length of approximately a thousand filopodia.

To compute the proportion of filopodia sampled in the explored regions, we measured the contour length of 45 sampled areas and multiplied it by the filopodial linear density obtained by Paez et al. (2017) from the same images. We estimated that half the filopodia population within the inspected areas were roughly sampled. We summarized the image analysis statistics in Table 2.

Analysis of filopodial lengths in cultured PC3 cells suggest two cell populations

We analyzed more than a thousand filopodia profiles from which we recovered 994 filopodial lengths in the range 0.5–15 µm. The average filopodial length for cultured PC3 cells was ~ 4 µm, which is similar to the lengths of filopodia in human lung adenocarcinoma cells (Liou et al. 2014), rat fibroblasts (Husainy et al. 2010) and neurites (Jontes et al. 2000). Figure 4a displays the obtained distribution; a quantitative description of the distribution in terms of it central moments is found in Table 3. The distribution is biased towards small length values and is long-tailed to the right

Table 2 Image analysis statistics

Symbol	Meaning	Value
N_{im}	No. of analyzed images	48
N_{cells}	No. of cells explored	226
N_{filo}	No. of measured filopodial lengths	994
$\hat{p}$	Estimated percentage of sampled filopodia	56%

Table 3 PC3 filopodial length statistics

Filopodia	N_{filo}	Mean (μm)	Std	Skewness	Excess kurtosis
All	994	4.1	1.9	1.7	3.9
>6	561	4.1	2.0	1.7	3.9
Group 1	319	3.4	1.1	0.6	0.6
Group 2	242	5.1	2.6	1.1	1.0

as both the skewness and excess kurtosis apart from zero. Similar distributions for filopodial lengths were reported in Jontes et al. (2000), Husainy et al. (2010).

We then wondered if this wide distribution of filopodial lengths results from local variability or it stems from a variability between different cells. To explore this, we analyzed the lengths of neighbor filopodia located within the same cell. To this end, we gathered the data coming from cells where we were able to successfully track 6 or more filopodia profiles ($N_{\text{filo}} = 561$ from $N_{\text{cells}} = 58$) to allow meaningful analysis. The resulting data (inset in Fig. 4a was representative of the total data set as reflected by the distribution statistical description shown in Table 3.

As an estimate of the dispersion of the filopodial lengths within single cells, we computed the standard deviation (SD) for each of the 58 cells (not shown) and

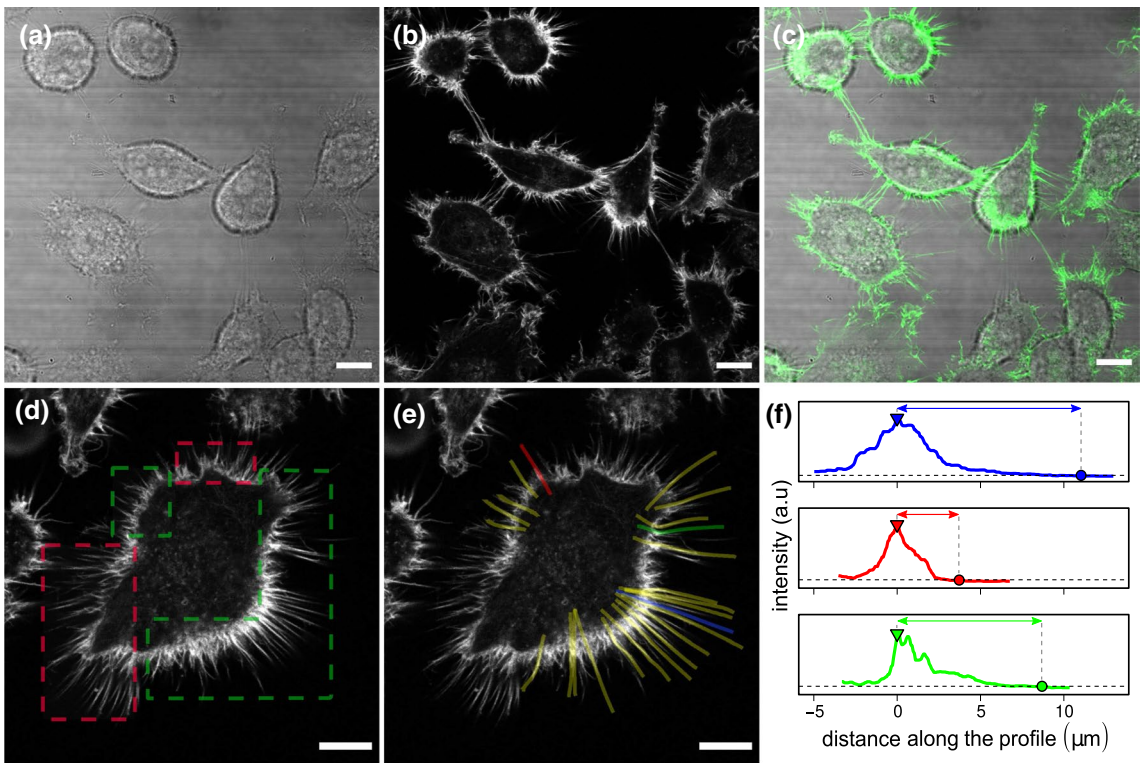

Fig. 3 Prostate tumor PC3 cells. **a** Phase contrast microscopy image. **b** Fluorescence microscopy image of the same viewfield (staining with rhodamine-phalloidin). **c** Merge of the fluorescence and phase contrast confocal images shown in (**a**, **b**). **d** Representative fluorescence image of PC3 cells. The regions of interest where filopodia are considered trackable are delimited by green shapes. The red rectangles surround regions where filopodia are considered unfit to be measured. In this case, the upper right red rectangle encloses a contact region and the lower left shape too, the latter also includes overlapping protrusions with intermittent intensity signal. **e** Lines indicate the filopodia that could be tracked (Scale bars: 10 μm). **f** Intensity smoothed profiles acquired from the lines traced in (**e**); the colours of the profiles correspond to the filopodia in (**e**). The filopodial tip locations are determined after selecting a threshold that considers background intensity (black dashed horizontal line). The triangles and circles represent the base and tip positions, respectively. The protrusion length is obtained by subtracting tip and base positions along the profile. Filopodial length of the protrusions covered by the blue, red and green lines in e are represented by lines with arrowheads of the respective colour. The smoothed profiles are horizontally shifted so that the filopodial base is at the origin

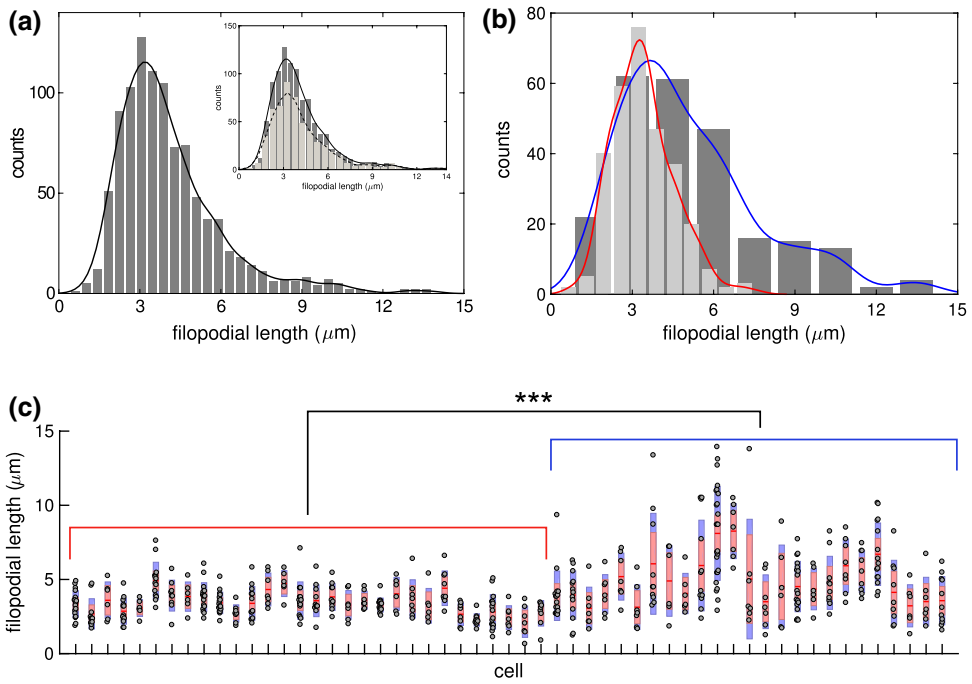

Fig. 4 **a** Distribution of filopodial length in cultured PC3 cells. Inset: comparison with the distribution of filopodial lengths sampled from cells where 6 or more filopodia could be tracked (light gray). The lines over the histograms represent re-normalized kernel density estimates. **b** Histograms of the filopodial lengths corresponding to Group 1 (light gray) and Group 2 (dark gray) (see main text). **c** Distribution of single cell data corresponding to Group 1 (red brackets) and Group 2 (blue brackets). The data obtained for each cell is shown accompanied by a boxplot (Campbell 2018) centered on its mean value. The pink and purple boxes represent the SEM and SD of the data, respectively. Asterisks indicate significant differences between the two groups according to a two-sample Kolmogorov–Smirnov test

found that their distribution deviates from normal according to a Shapiro–Wilk hypothesis test (p value $< 5 \times 10^{-5}$) (BenSaïda 2020). Thus, we classified the cells into two groups depending whether the SD of the lengths was less (Group 1) or greater (Group 2) than SD=1.3 µm. This threshold value roughly corresponds to the median of the SD distribution. The new distributions obtained for Group 1 ($N_{\text{filo}} = 319$) and Group 2 ($N_{\text{filo}} = 242$) are displayed in Fig. 4b, where we have also plotted the corresponding kernel density estimation. A quantitative description of the distributions in terms of their central moments can be found in Table 3. A two-sample Kolmogorov–Smirnov test showed that the two groups were significantly different (p value $< 10^{-14}$) supporting the presence of at least two different population of data. While one group of cells (Group 2) displays a wide distribution of lengths with very long filopodia, the other group (Group 1) shows a narrow and less biased distribution, with the absence of long processes.

At this point, we wonder if the presence of long (untracked) filopodia in a cell labeled as belonging to Group 1 could alter the statistical estimators determined for this group. In other words, such a cell would constitute a false positive according with our conclusions from Fig. 4. To avoid considering dubious data in subsequent analyzes, we decided to inspect again the images of cells corresponding to Group 1 and discard those cells with long filopodia that would have not been considered during the tracking procedure. To this end, a line separating a distance $d = 8\,\mu\text{m}$ from the cell perimeter was drawn and the number of filopodia exceeding this limit was inspected. Also, we estimated the length of long curled filopodia within this 8 µm-sized zone. This value of the length cutoff represented an upper bound for the Group 1 lengths, and thus filopodia longer than this value should represent outliers. This study revealed that only three of the considered cells displayed a least one filopodium longer than this threshold and, consequently they were discarded from further analysis.

Figure 4c displays the distribution of filopodial lengths within the remaining 55 individual cells, where we have intentionally sorted cells depending on the group they belong to. An inspection of this figure also evidences the differences between the two populations of filopodia previously remarked.

Interpretation of the experimental data using the stochastic model

When comparing the experimental data for PC3 cells with the results of the stochastic model, it led us to formulate two

questions. Can the stochastic model reproduce the experimental results for PC3 cells? What can we learn from that?

To answer to these questions, we first estimated the probability density functions of the filopodium lengths obtained from the stochastic model by performing a kernel density estimation. Some examples are shown in Fig. 5a, for five different values of v_r. We called E_1 and E_2 the experimental probability density functions for Groups 1 and 2, respectively, which are obtained from a kernel density estimation of the experimental data (see Fig. 4b). Then we propose to reconstruct E_1 and E_2 as a linear combination of the simulated distributions S_j, where the sub-index j stands for the jth retrograde velocity value:

$$E_1 = \sum_{j=1}^{m} C_j^1 S_j, \tag{1}$$

$$E_2 = \sum_{j=1}^{m} C_j^2 S_j, \tag{2}$$

C_j^1 and C_j^2 are the weight of the contribution of each theoretical distribution for Groups 1 and 2, respectively. We regard the same $m = 11$ values of retrograde velocity covering the range between 5 and 100 nm/s for both Eqs. 1 and 2.

We have shown in Table 3 that Groups 1 and 2 skewness and excess kurtosis apart from zero. Therefore, we use the first four moments of E_1, E_2 and S_j to calculate the coefficients C_j^1 and C_j^2, as discussed in Section "Reconstruction of

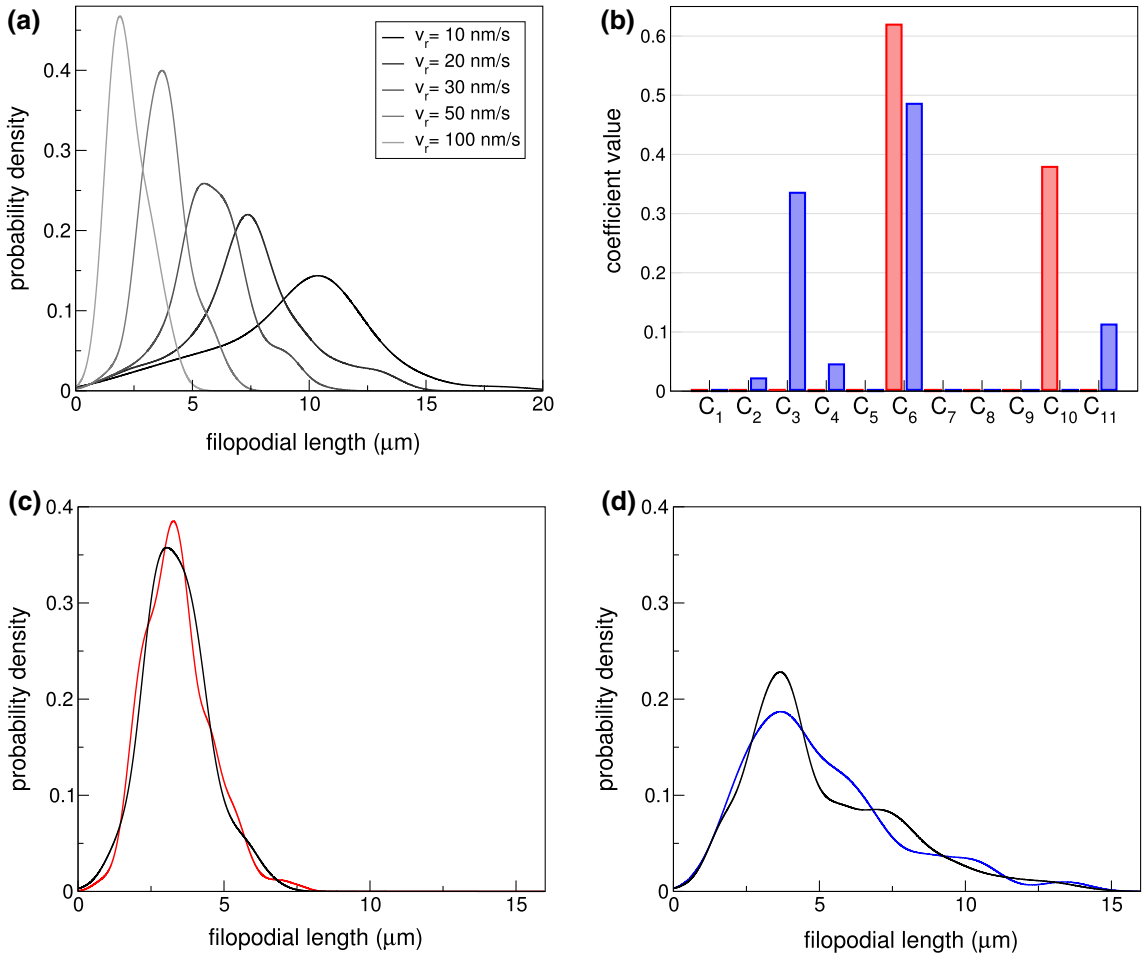

Fig. 5 Comparison between experimental and simulation data using 4 moments of the distributions. **a** Probability density functions of the theoretical filopodium lengths for different values of retrograde velocity as indicated in the legend, obtained from kernel density estimations. **b** Coefficients of Eqs. 1 and 2 for Groups 1 and 2 (red and blue, respectively). For Group 1 the coefficients C_j^1 whose contribution is greater than 2% are related to $v_r = 50$ and 90 nm/s ($C_1^3 < 0.002$, it is smaller than the line thickness). For Group 2, the non-null coefficients C_j^2 are associated to $v_r = 10, 20, 30, 50$ and 100 nm/s. **c**, **d** Experimental distributions E_1 and E_2 (red and blue lines, respectively), and the reconstructed simulation data by considering the coefficients shown in panel (**b**), for Groups 1 (**c**) and 2 (**d**)

the experimental filopodium length distributions". The coefficients obtained from Eqs. 1 and 2 are displayed in Fig. 5b. Figure 5c, d exhibits the reconstruction of E_1 and E_2 using these coefficients, which shows the good agreement between the model and the experimental data.

Note that contributions of v_r in the range 10–100 nm/s are necessary to reconstruct Group 2 distribution, while Group 1 distribution can be recovered with v_r values between 50 and 90 nm/s (by only considering contributions with weights greater than 2%). This result is related to the dispersion of the length values, which is greater in the case of Group 2 (see Table 3). Also, there is a predominance of low and medium values of v_r for Group 2, that is, $v_r = 20$ and 50 nm/s ($C_2^3 + C_2^6 > 80\%$). For Group 1, the emphasis is in medium and high values, that is, $v_r = 50$ and 90 nm/s ($C_1^6 + C_1^{10} > 98\%$). Since lower values of v_r are associated with higher values of filopodial length, the result above responds to the fact that Group 2 presents a long-tailed distribution biased to high length values.

Therefore, the main lesson from the comparison between the experimental data for PC3 cells and the stochastic model is that the reconstruction of Group 2 data involves a wide range of values of v_r, and that the main contributions come from low v_r values.

Discussion

Filopodia play key roles in several cellular processes such as sensing and migration (Mattila and Lappalainen 2008; Heckman and Plummer 2013; Sasaki et al. 2004); they are also involved in cell–cell interactions (Cohen et al. 2010; Paez et al. 2017; Miller et al. 1995; Sanders et al. 2013). Consequently, filopodia have a very rich phenomenology, with lengths, growth and retraction rates, and lifetimes, highly variable (Paul et al. 2015; Jang et al. 2010; Arjonen et al. 2014). The mechanisms underlying formation, maintenance and dynamics of filopodia are complex and not yet fully understood. To shed some light on the growth dynamics of filopodia, we proposed a cross-talk between a theoretical stochastic model and experiments in PC3 cells.

We studied filopodia patterns in non-confluent PC3 cell cultures using confocal microscopy. Cells were fixed and inmunolabelled with rhodamine phalloidin, allowing the visualization of actin structures. In some cases, filopodia take the form of cell–cell bridges (Bornschlögl 2013; Hoelzle and Svitkina 2012; Sanders et al. 2013) implicated in the transport and interchange of molecules or vesicles. These structures are very stable and it has been suggested that they are reminiscent structures that remained after the retraction of the lamellipodia of two adjacent cells that were previously in contact (Hoelzle and Svitkina 2012). We did not consider these kind of filopodial structures in this work. Rather, we focused on cell regions where single filopodia could be univocally tracked. We measured the lengths of these filopodia from the images using custom-made tracking routines and determined their distribution.

Since filopodia can grow and stabilize or decrease in response to external stimuli, their spatio-temporal patterns may contain information on the underlying signaling processes. It can be hypothesized that the distribution of filopodial lengths would provide information not only about the current scenario but also of the history and/or the heterogeneity of the environment in which the cell is immersed. Thus, we suggest that the signaling features could be inferred from the filopodia pattern.

Our analysis of the experimental results suggested the presence of two populations of cell regions according to the dispersion of their filopodial lengths, which we called Group 1 and Group 2. While Group 1 cells had filopodia with a narrow distribution of lengths, Group 2 showed a much more variable pattern. Up to our knowledge, our work is the first report on the presence of two different populations of filopodia in prostate tumor cells. This result reveals the presence of cellular heterogeneity that could be related to molecular noise (Huang 2009). It should be noted that specific subtypes of filopodia with distinct properties have been found in other cell systems (Paul et al. 2015; Jang et al. 2010; Arjonen et al. 2014). For instance, the sensing mechanism allowing neurite orientation involves two filopodia populations differing in their stability and adhesion properties, resulting in distinct filopodial length distributions (Jang et al. 2010). It has been argued that the presence of these two populations may allow to sense topographical extracellular matrix cues. Moreover, the motor protein Myosin-X promotes cell adhesion and migration by stabilizing filopodia that protrude into the extracellular matrix using the cell adhesion receptor $\beta 1$ integrin inducing the formation of long filopodia in different cell types (Arjonen et al. 2014). It has been reported that $\beta 1$ integrin trafficking can promote dynamic actin spike protrusion, known as FHOD3 (Paul et al. 2015), whose dynamics differ from other formin-dependent filopodial protrusions (Shibue et al. 2013) suggesting that the properties of the two filopodial subtypes may be very different (Paul et al. 2015; Jacquemet et al. 2019). This is specially relevant in cancer cells since Myosin-X is highly expressed in aggressive cancer subtypes (Arjonen et al. 2014; Peckham 2016). These examples show that the spatio-temporal characteristics of filopodia are intimidatingly related to the underlying signaling mechanisms.

Our experimental results were interpreted in terms of a stochastic model of filopodial growth that considers explicitly the main chemical reactions at the filament barbed end: polymerization and depolymerization of actin, as well as binding and unbinding of the regulatory proteins capping

and formin. Also, the processes that result in the centripetal movement of actin filaments are represented in the model by an effective retrograde velocity. We inspected the effect of varying the retrograde velocity on the filopodial length and we found an inverse nonlinear dependence between them.

Considering these results, we proposed that the experimental lengths obtained for PC3 cells could be approximated to a linear combination of the in silico results for different values of retrograde velocities. To assess the reconstructed distribution, we compared its first 4 moments with the corresponding experimental ones. We found a good agreement between the model and the experimental data. We concluded that the reconstruction of Group 2 data demanded a wider range of values of v_r than Group 1 reconstruction, for which also low values of v_r were absent.

Based on these results, we proposed that Group 2 data came from cell regions where heterogeneous signaling induced further variability in the retrograde flow velocity or filopodia stability (Gallo and Letourneau 2004; Jacquemet et al. 2016, 2019; Liou et al. 2014) resulting in long filopodia and a wide length distribution. Indeed, we note that in our experimental set-up cells are able to migrate before the fixation procedure takes place. During their migration, transient cell–cell contacts occur (Vasioukhin et al. 2000). We hypothesize that these sporadic encounters could also produce a heterogeneous signaling environment that would result in distinct filopodial dynamics.

Finally, micro-environment stiffness may regulate filopodial activities (Jang et al. 2010; Jacquemet et al. 2015; Aberle 2019). For instance, lung cancer cells cultured on softer substrates appeared to have longer filopodia, and slower filopodial retraction rates (Liou et al. 2014), both effects regulated by myosin II motors, suggesting an adhesion strength modulation in the cells. Our in vitro experiments were performed with prostate tumor cells growing on plastic culture wells previously coated with FNC coating mix. Of note, when imaging cells through confocal microscopy, only the most central areas were photographed, where we expect the distribution of the coating mix to be homogeneous. Thus, we rule out that the different filopodia populations observed in our experiments were originated by heterogeneities in the substrate stiffness.

Although we cannot measure the retrograde flow in our current set up since we treat with fixated cells, it would be possible to ascertain its value (at least indirectly) in experiments that allow recording the dynamics of filopodial growth, as reported in Bornschlögl (2013); Bornschlögl et al. (2013); Jang et al. (2010). Even more, if in those experiments the extracellular guidance cues (Heckman and Plummer 2013; Gallo and Letourneau 2004) and/or the cell signaling pathways (Saha et al. 2016; Jacquemet et al. 2016) were evaluated, they would constitute a strong test to our model.

In summary, the mechanical and topological properties of the substrate combined with cell-intrinsic factors and chemotactic cues will determine the filopodial patterns. Exploring the mechanisms that produce the population heterogeneity in prostate tumor cells will be the scope of future experiments.

Materials and methods

Numerical simulations

We implemented an off-lattice one dimensional stochastic model of filopodial growth. We model growth dynamics of already initiated protrusions. A simulated filopodium consists of several actin filaments, in our model the maximum number of filaments contained by a filopodial bundle is 16. The filaments' double helical conformation is simplified as single one-dimensional structures. Each filament is an assembly of sub-units of size δ and is considered to be independent of the other filaments within the protrusion. As the computational model is one-dimensional, we do not consider filaments radial distribution.

To simulate reactions and diffusion we apply a stochastic molecular approach. Results obtained with this method are expected to be equivalent to the ones found with the Gillespie algorithm, as shown by Erban at al. for a simpler model (Erban et al. 2014). The model implemented here is similar to the proposed by Zhuravlev and Papoian (2009). It takes into account the following main components: (1) diffusion of molecules from the cell body into the filopodium compartment, (2) polymerization and depolymerization, (3) actin-binding regulatory proteins and (4) retrograde flow.

Let us consider a filopodium at time t composed of $N(t)$ actin filaments of length $h_i(t), ;i = 1, 2, \ldots, N(t)$. We define the filopodial length $H(t) = \max(h_i)$ and consider the membrane position to be located $L/2 = 25$ nm above the longest filament $M(t) = H(t) + L/2$. A simulation time-step can be summarized as follows: (i) actin, formin and capping molecules can diffuse from the cytosol to the filopodia; (ii) all G-actin molecules whose position are between $[h_i(t) - L/2, h_i(t) + L/2]$ have a non-zero probability of polymerizing at the *ith* filament, with on-rate values according to the presence of a formin and/or a capping molecule at the barbed end. For each actin polymerized, the filament length is increased by δ; (iii) each of the actin molecules at the barbed end can depolymerize; (iv) all the formin/capping molecules whose position are between $[h_i(t) - L/2, h_i(t) + L/2]$ can bind into the barbed end of the *ith* filament (in the case that a formin/capping protein is not yet bound). Just one formin/capping can bind to the filament; (v) If there is a formin/capping bound to the filament, it can unbind; (vi) the filament length is reduced by the retrograde flow with a constant velocity v_r. Steps (ii)–(vi)

are performed for each of the $N(t)$ filaments. The filopodial length is updated taking the value of the longest filament.

The simulation time-step was chosen so that all the probabilities are significantly smaller than 1 to guarantee stochasticity ($\delta t = 10^{-6}$ s) and the algorithm was implemented in C programming language.

Diffusion The diffusive molecules contemplated by our model are G-actin, capping protein and formin. The three types of biomolecules are present in the cytoplasm with different cytosolic concentrations (see Table 1), they follow one-dimensional Brownian motion dynamics in the axial direction and enter into the filopodial tube stochastically. G-actin, formin and capping protein diffusion into and within the filopodium is implemented in the same way Erban et al. did for G-actin (Erban et al. 2014) as we describe below.

G-actin is introduced into the filopodial structure with probability $\frac{2N^{\text{act}}}{L}\sqrt{\frac{D_{\text{act}}\delta t}{\pi}}$, where $N^{\text{act}} = 5.3$ is the number of G-actin molecules within the volume V of a cylinder of height $L = 50$ nm and diameter $d = 150$ nm and is calculated by multiplying the bulk concentration $[A]_{cyt}$ by V. The initial position of a molecule introduced into the filopodium is sampled from the probability density function $f(x) = \sqrt{\frac{\pi}{4D_{\text{act}}\delta t}}\, erfc\left(\frac{x}{\sqrt{4D_{\text{act}}\delta t}}\right)$ (Erban et al. 2014). Formin and capping protein diffusive jumps into the filopodium are implemented likewise with the corresponding parameters (see Table 1), in these cases $N^{\text{form}} = 0.042$ and $N^{\text{cap}} = 0.026$. Flegg et al. (2011, (2014) provide a detailed description of the implementation of diffusive jumps from a bulk domain (cytosol) into a molecular domain (filopodium).

All the molecules trajectories are explicitly computed. At time t, within the filopodium there are $n^{\text{act}}(t)$ G-actin molecules at positions $x_j^{\text{act}}(t),\ j = 1, 2, \ldots, n^{\text{act}}(t)$, $n^{\text{cap}}(t)$ capping proteins located at $x_k^{\text{cap}}(t),\ k = 1, 2, \ldots, n^{\text{cap}}(t)$ and $n^{\text{form}}(t)$ formin molecules placed at $x_l^{\text{form}}(t),\ l = 1, 2, \ldots, n^{\text{form}}(t)$. The position of each particle can take values in a continuous range between the filopodial base and the membrane position $[0, M(t)]$.

All the molecules positions evolve as random walk particles; hence, an mth molecule located in $x_m(t)$ at time t moves to the position $x_m(t + \delta t) = x_m(t) + \delta x_m$, where the spacial step $\delta x_m = \text{RMS} \times \epsilon_m$, RMS is the root mean square displacement in 1D $\left(\sqrt{2D\delta t}\right)$ and ϵ_m is a standard normal distributed random number. Reflective boundary conditions were imposed at the membrane, if $x_m(t) + \delta_m > M(t)$ then $x_{\text{m}}(t + \delta t) = M(t) - \left(x_m(t) + \delta x_m - M(t)\right)$ and open boundary conditions were set at the filopodial base, if $x_m(t + \delta t) < 0$ then the particle is removed from the system and the number of that type of molecules within the filopodial structure is reduced by one.

(De) Polymerization At time t a filopodium consists of $N(t)$ filaments of length $h_i(t),\ i = 1, 2, \ldots, N(t)$. Each one of the filaments evolves with its own independent dynamics. Since we perform stochastic molecular simulations (Erban et al. 2014), for all the filaments we consider that each individual G-actin molecule located at a distance smaller than $L/2$ from the filament tip (Lan and Papoian 2008) can polymerize into its barbed end. In order to determine the assembling probability of each actin monomer, we must consider the rate of G-actin polymerization, $k_{\text{on}}^{\text{act}}$, in units of $\left[\text{s}^{-1}\right]$ instead of $\left[\mu\text{M}^{-1}\text{s}^{-1}\right]$ as usually reported (see Table 1). Therefore, we take the volume of a cylinder of height L and diameter d and we get the parameter in the desired units $K_{\text{on}}^{\text{act}} = 21.9s^{-1}$ per molecule of G-actin (note the use of capital letter for the variable in units of s^{-1}). Accordingly, the assembling probability for each G-actin molecule within a time interval (δt) is $K_{\text{on}}^{\text{act}} \times \delta t$. The case where there is a formin and/or a capping molecule bound to the filament will be discussed next.

Because we model the microfilaments as single one-dimensional objects, while they actually are double helices, the filaments increase its lengths by half the size of an actin monomer (δ) when polymerization occurs. Next, we remove the polymerized G-actin protein from the pool of free molecules. Moreover, within a time interval (δt) each filament has a depolymerizing probability of $k_{\text{off}}^{\text{act}} \times \delta t$, as $k_{\text{off}}^{\text{act}}$ is the dissociation rate of an actin monomer at the barbed end. If a depolymerization event happens the filament length is reduced by δ and a new G-actin monomer is introduced at the position of the filament length before depolymerizing $h_i(t)$. See Fig. 6a for a schematic representation of G-actin assembly and disassembly (yellow arrows).

Actin-binding regulatory proteins Two types of actin-binding proteins are contemplated by the model: formin and capping proteins. In the same way that polymerization was implemented, for each actin filament, all the formin and capping molecules located at a distance less than $L/2$ can attach to the filament with the appropriate probability. To calculate these probabilities, the units of the on-rates were transformed from $\left[\mu\text{M}^{-1}\text{s}^{-1}\right]$ to $\left[\text{s}^{-1}\right]$, as it was done with the polymerization rate $k_{\text{on}}^{\text{act}}$. Thereby we obtain $K_{\text{on}}^{\text{act-form}} = 100\text{s}^{-1}$, $K_{\text{on}}^{\text{form}} = 54.9\text{s}^{-1}$, $K_{\text{on}}^{\text{form-cap}} = 3.02\text{s}^{-1}$, $K_{\text{on}}^{cap} = 24.2\text{s}^{-1}$ and $K_{\text{on}}^{\text{cap-form}} = 0.27\text{s}^{-1}$. Again, note the use of capital letters when the variables are in units of s^{-1}.

In the case of free filament barbed ends, in addition to G-actin polymerization and depolymerization, two other events are possible: formins can bind with probability $K_{\text{on}}^{\text{form}} \times \delta t$, or capping proteins can bind with probability $K_{\text{on}}^{\text{cap}} \times \delta t$ (green and red arrows in Fig.6a, respectively). When a filament barbed end is capped both polymerization and depolymerization are completely blocked. In this situation there are two possibilities, formin can bind to the capped barbed end with probability $K_{\text{on}}^{\text{form-cap}} \times \delta t$, or uncapping can take place with probability $k_{\text{off}}^{\text{cap}} \times \delta t$ (green and red arrows in Fig.6b, respectively). When a filament is anticapped with formin the

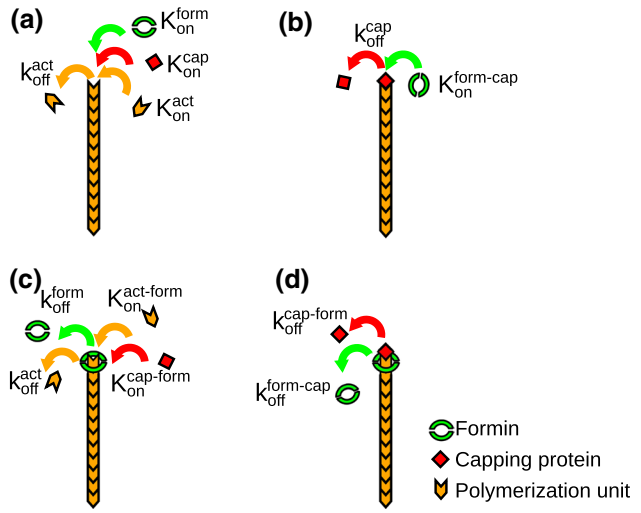

Fig. 6 Illustration of the stochastic events at the filaments barbed ends. According to our model, there are four states in which a filament can be found and the dynamics is different depending on the case. **a** Free barbed end: an actin monomer can be depolymerized from the filament with rate k_{off}^{act}, a G-actin molecule can be polymerized with rate K_{on}^{act}, a formin or a capping protein can bind to the barbed end with rates K_{on}^{form} and K_{on}^{cap}, respectively. The occurrence of one of the last two events alters the kinetics of the filament as described below. **b** Capped barbed end: the capping protein entirely inhibits de/polymerization at the barbed end and the events that can take place are uncapping with rate k_{off}^{cap} or the binding of formin with rate $K_{on}^{form-cap}$. **c** Formin anticapped barbed end: formin can be unbound or an actin monomer depolymerized with rates k_{off}^{form} and k_{off}^{act}, respectively. G-actin assembles with rate $K_{on}^{act-form}$ $\left(> K_{on}^{act}\right)$ or a capping protein can bind with rate $K_{on}^{cap-form}$, leading to the situation in *d*. **d** Capping protein and formin simultaneously bound: The capping protein blocks polymerization and depolymerization and the regulatory proteins can be released with rates $k_{off}^{cap-form}$ or $k_{off}^{form-cap}$ for capping and formin, respectively. The arrows represent binding or polymerizing events if they point towards the filament or release events if they point out of the filament. The colors of the arrows indicate the molecule that binds or releases

polymerization probability is $K_{on}^{act\text{ - }form} \times \delta t$ whilst depolymerization remains unaltered (yellow arrows in Fig.6c). Besides, a capping protein can bind to a formin-bound barbed end with probability $K_{on}^{cap-form} \times \delta t$, or the formin can unbind with probability $k_{off}^{form} \times \delta t$ (red and green arrows in Fig.6c, respectively). Finally, when a filament has both a formin and a capping protein attached to its barbed end at the same time, polymerization is prevented by the capping protein. In this case, the capping protein can unbind with probability $k_{off}^{cap-form} \times \delta t$, or the formin can unbind with probability $k_{off}^{form-cap} \times \delta t$ (red and green arrows in Fig. 6d, respectively). In analogy with the G-actin dynamics implementation, when a formin or a capper binds to a filament barbed end the protein is removed from its respective pool and the number of the corresponding type of molecule is reduced by one. In addition, when unbinding occurs the new unbound protein is introduced into the system of free molecules in the same way that we did for G-actin when a depolymerization event took place.

Retrograde flow Microfilaments pointed end depolymerization together with the action of myosin leads to the phenomenon of retrograde flow, a centripetal movement of actin filaments. Our model assumes all the filaments that conform a filopodial bundle move backwards with the same constant retrograde velocity v_r. At every time-step δt each filament of length $h_i(t)$ is shortened by $v_r \times \delta t$; therefore, $h_i(t + \delta t) \rightarrow h_i(t) - v_r \times \delta t$.

Statistical analysis

The filopodial length averaged over an ensemble of n simulation runs at time t is defined as

$$\langle L(t) \rangle = \frac{1}{n} \sum_{i=1}^{n} L_i(t), \tag{3}$$

where $L_i(t)$ is the length of the realization i at time t. Obviously, the n realizations refer to the same parameters values. Further, the mean filopodial length is defined as the time average of $\langle L(t) \rangle$ over T values:

$$\overline{L} = \frac{1}{T} \sum_{t=1}^{T} \langle L(t) \rangle. \tag{4}$$

Since we choose a sampling time of 1s, T is the maximum time considered (in s).

To calculate $\overline{L}$ (shown in Fig. 2b), we consider n different runs of $T = 1000$ s, with a time step of 1s. For v_r between 20 and 100 nm/s we use $n = 5$, whereas for $v_r = 5$ nm/s and $v_r = 10$ nm/s, we take $n = 18$ and 17, respectively. Better statistics are necessary to represent low v_r data because of large fluctuations in the transient period. The same simulation data were used to calculate the probability density functions S_j (Step 2 of Section "Reconstruction of the experimental filopodium length distributions").

In cases where binning was required, the size of the bins was determined by Freedman–Diaconi's rule. Boxplots are presented as mean, SEM and SD, according to Campbell (2018). For the filopodial length analysis, distributions were compared with a two-sample Kolmogorov–Smirnov test. A kernel density estimation was applied to the data to obtain probability density estimate curves.

Cell culture, sample preparation for imaging and confocal microscopy

PC3 cells were obtained from the American Type Culture Collection (Manassas, VA, USA) and were routinely cultured in RPMI 1640 (Invitrogen, Grand Island, NY, USA) supplemented with 10% fetal bovine serum (FBS), penicillin

100 U/mL, streptomycin 100 g/mL and amphotericin 0.5 g/mL. Cells were cultures in cell culture plates previously coated with FNC coating mix (Athena Enzyme Systems, USA). The procedure involved: (1) adding 0.2 mL of FNC Coating Mix per square centimeter of surface area of the culture vessel, allowing the surface to be completely covered with a layer of liquid; (2) incubating for 30 s at room temperature and removing the coating mix with a pipet prior to cell seeding. As described by the manufacturer this mix is a serum-free tissue culture reagent that contains fibronectin, collagen and albumin that is used to enhance the attachment of cells to plastic flasks or microplates. The formula resembles the extracellular matrix (ECM), hence mimicking the ECM and favoring the rate of cell attachment to any plastic substratum. The rhodamine-phalloidin was purchased from Life Technologies (Thermo Fisher Scientific Inc., Eugene, OR, USA). Immunofluorescence experiments and quantitative microscopy: PC3 cells were fixed with 8% paraformaldehyde (PFA) (20 min, room temperature) and stained with rhodamine phalloidin (1 h, room temperature) (Paez et al. 2017). Confocal images were acquired by confocal microscopy (FV1000, Olympus, Tokyo, Japan) using an UPlanSApo 60x oil immersion objective (NA 1/41.35; Olympus), a diode laser of 543 nm as the excitation source and fluorescence was collected in the range of 555–655 nm.

Filopodia localization and tracking

Image processing was done with ImageJ and data analysis was carried out with R. The workflow to determine filopodial length involved manual tracking of filopodia and the latter automatic determination of its length. Image contrast and brightness were adjusted for better identification of filopodia. Protrusions that did not accomplish certain minimal requirements were not measured as stated before.

We acquired intensity profiles of lines traced above the filopodia using the ImageJ line profile tool in segmented mode, line width was established considering image resolution so that each filopodium was completely covered by the line (7 pixels for 1 image, 8 pixels for 8 images and 10 pixels for the remaining 39).

The program computes the average intensity along the line. The line starting point was set inside the cell body and the ending point was placed beyond the visible tip as shown in Fig.3e. We also acquired background intensity profiles for every image. Each filopodium and cell was assigned an ID number, and for every cell we also kept information if it had contacts or not with surrounding cells. All the objects were saved within the images so that every filopodium can be tracked back.

The recovered intensity profiles showed a rapid rising until reaching a maximum around the filopodial base and the subsequent gradual decrease until reaching the filopodial extreme where the signal becomes indistinguishable from the statistical background noise (Fig.3f). Then each intensity profile was smoothed with the R smooth function, a median filter to reduce the noise signal. We set the pixel with the highest intensity as base of the filopodia. We performed statistical analysis on the background intensity profiles for every image, determining the mean background signal and its standard deviation. The tip of the structure was determined by setting a threshold as the mean plus 3 standard deviations of the background signal. We obtained filopodial length subtracting the tip to the base position.

We aimed to estimate the sampled filopodia percentage from the total population within the explored regions. For that, we measured the contour length of 45 sampled areas (≈ 1194 μm) and multiplied it by the filopodial linear density ($\approx 0.5\ \mu m^{-1}$) (Paez et al. 2017). This led to ≈ 597 expected filopodia in contrast to 337 ones within the covered perimeter. Therefore, we estimated to have measured the length of about $\approx 56\%$ of the protrusions within the explored areas.

Reconstruction of the experimental filopodium length distributions

As we stated in Section "Interpretation of the experimental data using the stochastic model", the probability density function of the filopodium length for Groups 1 and 2 obtained from experimental data can be reconstructed by a linear combination of the simulated distributions obtained for different values of retrograde velocity v_r. To determine the weight of each simulation distribution in the reconstruction of the experimental data, the procedures are detailed below.

Step 1. We use the kernel density estimation to generate two distributions, E_1 and E_2, for the experimental filopodium lengths for Groups 1 and 2, respectively.

Step 2. We use the kernel density estimation to generate m length distributions from the simulation data, each one corresponding to a different value of v_r. Let us call these distributions as S_j, with $j = 1, \ldots, m$. For the simulations we consider the following $m = 11$ values of retrograde velocity, $v_r = 5, 10, 20, 30, 40, 50, 60, 70, 80, 90, 100$ n m / s. Information about the simulation data considered to construct the functions S_j are detailed in Section "Statistical analysis".

Step 3. To reconstruct the experimental distributions E_1 and E_2, we should determine the weights C_j^1 and C_j^2 of each simulation distribution S_j, for Groups 1 and 2,

Table 4 Moments of the experimental distributions, E_1 and E_2

	1st	2nd	3rd	4th
Group 1	$\mu_1^1 = 3.4$	$\mu_2^1 = 13.0$	$\mu_3^1 = 54.5$	$\mu_4^1 = 250$
Group 2	$\mu_1^2 = 5.1$	$\mu_2^2 = 33.0$	$\mu_3^2 = 260$	$\mu_4^2 = 2375$

respectively, that is, $E_1 = \sum_{j=1}^{m} C_j^1 S_j$ and $E_2 = \sum_{j=1}^{m} C_j^2 S_j$ (Eqs. 1 and 2, respectively).

Step 4. The moments of order i, μ_i, with $i = 1, \ldots, 4$ are calculated for the experimental distributions E_1 and E_2 (see Table 4). Therefore, we can define $\overrightarrow{M_1} = \left(\mu_1^1, \mu_2^1, \mu_3^1, \mu_4^1\right)$ and $\overrightarrow{M_2} = \left(\mu_1^2, \mu_2^2, \mu_3^2, \mu_4^2\right)$, for Groups 1 and 2, respectively.

Step 5. We compute the moments of order i, μ_i, with $i = 1, \ldots, 4$, for each of the S_j simulated data performed for different retrograde velocities values: $\overrightarrow{M_{S_j}} = \left(\mu_1^{S_j}, \mu_2^{S_j}, \mu_3^{S_j}, \mu_4^{S_j}\right)$, with $j = 1, \ldots, m$.

Step 6. We consider the following linear regression for each of the moments of Group 1:

$$\begin{aligned}
\mu_1^1 &= C_1^1 \mu_1^{S1} + C_2^1 \mu_1^{S2} + \cdots + C_m^1 \mu_1^{Sm}, \\
\mu_2^1 &= C_1^1 \mu_2^{S1} + C_2^1 \mu_2^{S2} + \cdots + C_m^1 \mu_2^{Sm}, \\
\mu_3^1 &= C_1^1 \mu_3^{S1} + C_2^1 \mu_3^{S2} + \cdots + C_m^1 \mu_3^{Sm}. \\
\mu_4^1 &= C_1^1 \mu_4^{S1} + C_2^1 \mu_4^{S2} + \cdots + C_m^1 \mu_4^{Sm}.
\end{aligned} \tag{5}$$

Similar equations are found for Group 2.

Step 7. Let us normalize the moments of the experimental distributions respect to the first moment as

$$\overrightarrow{M_1^R} = \left(\mu_1^1/\mu_1^1, \mu_2^1/\left[\mu_1^1\right]^2, \mu_3^1/\left[\mu_1^1\right]^3, \mu_4^1/\left[\mu_1^1\right]^4\right),$$
$$\overrightarrow{M_2^R} = \left(\mu_1^2/\mu_1^2, \mu_2^2/\left[\mu_1^2\right]^2, \mu_3^2/\left[\mu_1^2\right]^3, \mu_4^2/\left[\mu_1^2\right]^4\right).$$

Therefore, Eq. 5 for Group 1 and similar equations for Group 2 can be rewrite (in a reduced way) as

$$\mu_i^1/\left[\mu_1^1\right]^i = \sum_{j=1}^{m} C_j^1 \mu_i^{Sj}/\left[\mu_1^1\right]^i, \tag{6}$$

$$\mu_i^2/\left[\mu_1^2\right]^i = \sum_{j=1}^{m} C_j^2 \mu_i^{Sj}/\left[\mu_1^2\right]^i, \tag{7}$$

with $i = 1, \ldots, 4$.

This normalization procedure is necessary to give similar importance to the different moments when the regression analysis is done. In other way, high moments will be favored.

Step 8. We determine the coefficients $\overrightarrow{C^1} = \left(C_1^1, C_2^1, C_3^1, \ldots, C_m^1\right)$ and $\overrightarrow{C^2} = \left(C_1^2, C_2^2, C_3^2, \ldots, C_m^2\right)$, associated with the constrains given by Eqs. 6 and 7, respectively. The system has no exact solution;therefore, we use a L1 minimization (Roos et al. 2005) to obtain $\overrightarrow{C^1}$ and $\overrightarrow{C^2}$.

Step 9. After the determination of C_j^1 and C_j^2 we normalize the coefficients $\sum_{j=1}^{m} C_j^1 = 1$ and $\sum_{j=1}^{m} C_j^2 = 1$ to ensure the normalization of the reconstructed distributions.

Acknowledgements We thank Luis Diambra for helpful discussions on the method to reconstruct the experimental distributions. We thank Carla Pallavicini for valuable advise on image analysis.

Author contributions LB and NG designed study, DS, LB and NG analyzed data, DS, AP, GG, LB and NG performed research, DS, LB and NG wrote the paper. LB and NG contributed equally to this study.

Compliance with ethical standards

Conflict of interest The authors declare that they have no conflict of interest or competing interests.

Ethics approval Not applicable.

Funding We acknowledge support from the Agencia Nacional de Promoción Científica y Tecnológica (PICT 2015-0370 and PICT-RAICES-2018-02639), Argentina.

Consent to participate All the authors consent to participate.

Consent for publication All the authors consent for publication.

Code availability All the codes used in this work are available on request to the corresponding authors.

References

Aberle H (2019) Axon guidance and collective cell migration by substrate-derived attractants. Front Mol Neurosci 12:148

Anderson TW, Vaughan AN, Cramer LP (2008) Retrograde flow and myosin ii activity within the leading cell edge deliver f-actin to the lamella to seed the formation of graded polarity actomyosin ii filament bundles in migrating fibroblasts. Mol Biol Cell 19(11):5006–5018

Arjonen A, Kaukonen R, Mattila E, Rouhi P, Högnäs G, Sihto H, Miller BW, Morton JP, Bucher E, Taimen P et al (2014) Mutant p53-associated myosin-x upregulation promotes breast cancer invasion and metastasis. J Clin Investig 124(3):1069–1082

Atilgan E, Wirtz D, Sun SX (2006) Mechanics and dynamics of actin-driven thin membrane protrusions. Biophys J 90(1):65–76

BenSaïda A (2020) Shapiro-wilk and shapiro-francia normality tests . https://www.mathworks.com/matlabcentral/fileexchange/13964-shapiro-wilk-and-shapiro-francia-normality-tests. MATLAB Central File Exchange. Retrieved 15 July 2020

Bornschlögl T (2013) How filopodia pull: what we know about the mechanics and dynamics of filopodia. Cytoskeleton 70(10):590–603

Bornschlögl T, Romero S, Vestergaard CL, Joanny JF, Van Nhieu GT, Bassereau P (2013) Filopodial retraction force is generated by

cortical actin dynamics and controlled by reversible tethering at the tip. Proc Natl Acad Sci 110(47):18928–18933
Breitsprecher D, Koestler SA, Chizhov I, Nemethova M, Mueller J, Goode BL, Small JV, Rottner K, Faix J (2011) Cofilin cooperates with fascin to disassemble filopodial actin filaments. J Cell Sci 124(19):3305–3318
Campbell R (2018) notBoxPlot. https://github.com/raacampbell/notBoxPlot, GitHub. Retrieved 18 Dec 2018
Cohen M, Georgiou M, Stevenson NL, Miodownik M, Baum B (2010) Dynamic filopodia transmit intermittent delta-notch signaling to drive pattern refinement during lateral inhibition. Dev Cell 19(1):78–89
Daniels D (2010) Effect of capping protein on a growing filopodium. Biophys J 98(7):1139–1148
Dominguez R, Holmes KC (2011) Actin structure and function. Anuu Rev Biophys 40:169–186
Erban R, Flegg MB, Papoian GA (2014) Multiscale stochastic reaction-diffusion modeling: application to actin dynamics in filopodia. Bull Math Biol 76(4):799–818
Flegg MB, Chapman SJ, Erban R (2011) The two-regime method for optimizing stochastic reaction-diffusion simulations. J R Soc Interface 9:859–868
Flegg MB, Chapman SJ, Zheng L, Erban R (2014) Analysis of the two-regime method on square meshes. SIAM J Sci Comput 36(3):B561–B588
Gallo G, Letourneau PC (2004) Regulation of growth cone actin filaments by guidance cues. J Neurobiol 58(1):92–102
Goode BL, Eck MJ (2007) Mechanism and function of formins in the control of actin assembly. Annu Rev Biochem 76:593–627
Heckman CA, Plummer H III (2013) Filopodia as sensors. Cell Signal 25(11):2298–2311
Hoelzle MK, Svitkina T (2012) The cytoskeletal mechanisms of cell-cell junction formation in endothelial cells. Mol Biol Cell 23(2):310–323
Huang S (2009) Non-genetic heterogeneity of cells in development: more than just noise. Development 136(23):3853–3862
Husainy AN, Morrow AA, Perkins TJ, Lee JM (2010) Robust patterns in the stochastic organization of filopodia. BMC Cell Biol 11(1):86
Jacquemet G, Hamidi H, Ivaska J (2015) Filopodia in cell adhesion, 3d migration and cancer cell invasion. Curr Opin Cell Biol 36:23–31
Jacquemet G, Baghirov H, Georgiadou M, Sihto H, Peuhu E, Cettour-Janet P, He T, Perälä M, Kronqvist P, Joensuu H et al (2016) L-type calcium channels regulate filopodia stability and cancer cell invasion downstream of integrin signalling. Nat Commun 7(1):1–17
Jacquemet G, Paatero I, Carisey AF, Padzik A, Orange JS, Hamidi H, Ivaska J (2017) Filoquant reveals increased filopodia density during breast cancer progression. J Cell Biol 216(10):3387–3403
Jacquemet G, Stubb A, Saup R, Miihkinen M, Kremneva E, Hamidi H, Ivaska J (2019) Filopodome mapping identifies p130cas as a mechanosensitive regulator of filopodia stability. Curr Biol 29(2):202–216
Jang KJ, Kim MS, Feltrin D, Jeon NL, Suh KY, Pertz O (2010) Two distinct filopodia populations at the growth cone allow to sense nanotopographical extracellular matrix cues to guide neurite outgrowth. PLoS One 5(12):e15966
Jontes JD, Buchanan J, Smith SJ (2000) Growth cone and dendrite dynamics in zebrafish embryos: early events in synaptogenesis imaged in vivo. Nat Neurosci 3(3):231–237
Kapustina M, Vitriol E, Elston TC, Loew LM, Jacobson K (2010) Modeling capping protein frap and cali experiments reveals in vivo regulation of actin dynamics. Cytoskeleton 67(8):519–534
Kovar DR, Wu JQ, Pollard TD (2005) Profilin-mediated competition between capping protein and formin cdc12p during cytokinesis in fission yeast. Mol Biol Cell 16(5):2313–2324
Kovar DR, Harris ES, Mahaffy R, Higgs HN, Pollard TD (2006) Control of the assembly of atp-and adp-actin by formins and profilin. Cell 124(2):423–435
Lan Y, Papoian GA (2008) The stochastic dynamics of filopodial growth. Biophys J 94(10):3839–3852
Lin CH, Espreafico EM, Mooseker MS, Forscher P (1996) Myosin drives retrograde f-actin flow in neuronal growth cones. Neuron 16(4):769–782
Liou YR, Torng W, Kao YC, Sung KB, Lee CH, Kuo PL (2014) Substrate stiffness regulates filopodial activities in lung cancer cells. PLoS One 9(2):e89767
Marchenko OO, Das S, Yu J, Novak IL, Rodionov VI, Efimova N, Svitkina T, Wolgemuth CW, Loew LM (2017) A minimal actomyosin-based model predicts the dynamics of filopodia on neuronal dendrites. Mol Biol Cell 28(8):1021–1033
Mattila PK, Lappalainen P (2008) Filopodia: molecular architecture and cellular functions. Nat Rev Mol Biol Cell 9(6):446–454
McCroskery S, Chaudhry A, Lin L, Daniels MP (2006) Transmembrane agrin regulates filopodia in rat hippocampal neurons in culture. Mol Cell Neurosci 33(1):15–28
McGrath JL, Tardy Y, Dewey C Jr, Meister J, Hartwig J (1998) Simultaneous measurements of actin filament turnover, filament fraction, and monomer diffusion in endothelial cells. Biophys J 75(4):2070–2078
McMillen LM, Vavylonis D (2016) Model of turnover kinetics in the lamellipodium: implications of slow-and fast-diffusing capping protein and arp2/3 complex. Phys Biol 13(6):066009
Medeiros NA, Burnette DT, Forscher P (2006) Myosin ii functions in actin-bundle turnover in neuronal growth cones. Nat Cell Biol 8(3):216–226
Miller J, Fraser SE, McClay D (1995) Dynamics of thin filopodia during sea urchin gastrulation. Development 121(8):2501–2511
Mogilner A, Rubinstein B (2005) The physics of filopodial protrusion. Biophys J 89(2):782–795
Oldenbourg R, Katoh K, Danuser G (2000) Mechanism of lateral movement of filopodia and radial actin bundles across neuronal growth cones. Biophys J 78(3):1176–1182
Paez A, Vazquez E, Gueron G (2017) Heme oxygenase 1 governs the cytoskeleton at filopodia: pulling the brakes on the migratory capacity of prostate tumoral cells. Cell Death Discov 3(1):1–2
Paul NR, Allen JL, Chapman A, Morlan-Mairal M, Zindy E, Jacquemet G, Fernandez del Ama L, Ferizovic N, Green DM, Howe JD et al (2015) $\alpha 5\beta 1$ integrin recycling promotes arp2/3-independent cancer cell invasion via the formin fhod3. J Cell Biol 210(6):1013–1031
Peckham M (2016) How myosin organization of the actin cytoskeleton contributes to the cancer phenotype. Biochem Soc Trans 44(4):1026–1034
Peskin CS, Odell GM, Oster GF (1993) Cellular motions and thermal fluctuations: the brownian ratchet. Biophys J 65(1):316–324
Pollard TD, Blanchoin L, Mullins RD (2000) Molecular mechanisms controlling actin filament dynamics in nonmuscle cells. Annu Rev Biophys Biomol Struct 29(1):545–576
Roos C, Terlaky T, Vial JP (2005) Interior point methods for linear optimization. Springer Science & Business Media, Boston, MA
Saha T, Rathmann I, Viplav A, Panzade S, Begemann I, Rasch C, Klingauf J, Matis M, Galic M (2016) Automated analysis of filopodial length and spatially resolved protein concentration via adaptive shape tracking. Mol Biol Cell 27(22):3616–3626
Sanders TA, Llagostera E, Barna M (2013) Specialized filopodia direct long-range transport of shh during vertebrate tissue patterning. Nature 497(7451):628–632

Sasaki AT, Chun C, Takeda K, Firtel RA (2004) Localized ras signaling at the leading edge regulates pi3k, cell polarity, and directional cell movement. J Cell Biol 167(3):505–518

Shekhar S, Kerleau M, Kühn S, Pernier J, Romet-Lemonne G, Jégou A, Carlier MF (2015) Formin and capping protein together embrace the actin filament in a ménage à trois. Nat Commun 6(1):1–12

Shibue T, Brooks MW, Weinberg RA (2013) An integrin-linked machinery of cytoskeletal regulation that enables experimental tumor initiation and metastatic colonization. Cancer Cell 24(4):481–498

Sinnar SA, Antoku S, Saffin JM, Cooper JA, Halpain S (2014) Capping protein is essential for cell migration in vivo and for filopodial morphology and dynamics. Mol Biol Cell 25(14):2152–2160

Steffen A, Faix J, Resch GP, Linkner J, Wehland J, Small JV, Rottner K, Stradal TE (2006) Filopodia formation in the absence of functional wave-and arp2/3-complexes. Mol Biol Cell 17(6):2581–2591

Svitkina TM, Bulanova EA, Chaga OY, Vignjevic DM, Kojima SI, Vasiliev JM, Borisy GG (2003) Mechanism of filopodia initiation by reorganization of a dendritic network. J Cell Biol 160(3):409–421

Tatavarty V, Das S, Yu J (2012) Polarization of actin cytoskeleton is reduced in dendritic protrusions during early spine development in hippocampal neuron. Mol Biol Cell 23(16):3167–3177

Vasioukhin V, Bauer C, Yin M, Fuchs E (2000) Directed actin polymerization is the driving force for epithelial cell-cell adhesion. Cell 100(2):209–219

Vitriol EA, McMillen LM, Kapustina M, Gomez SM, Vavylonis D, Zheng JQ (2015) Two functionally distinct sources of actin monomers supply the leading edge of lamellipodia. Cell Rep 11(3):433–445

Wolff K, Barrett-Freeman C, Evans MR, Goryachev AB, Marenduzzo D (2014) Modelling the effect of myosin x motors on filopodia growth. Phys Biol 11(1):016005

Zhuravlev PI, Papoian GA (2009) Molecular noise of capping protein binding induces macroscopic instability in filopodial dynamics. Proc Natl Acad Sci 106(28):11570–11575. https://doi.org/10.1073/pnas.0812746106. https://www.pnas.org/content/106/28/11570

Zhuravlev PI, Papoian GA (2011) Protein fluxes along the filopodium as a framework for understanding the growth-retraction dynamics: the interplay between diffusion and active transport. Cell Adhesion Mig 5(5):448–456